Journal of Alloys and Compounds 989 (2024) 174367

Contents lists available at ScienceDirect

Journal of Alloys and Compounds

journal homepage: www.elsevier.com/locate/jalcom

Research article

Structure relations with transport properties in p-type thermoelectric materials: Iron silicides

Sopheap Sam, Umar Farooq, Mizuki Namba, Kosuke Yamazaki, Hiroshi Nakatsugawa *

Graduate School of Engineering Science, Yokohama National University, Yokohama 240-8501, Japan

ARTICLE INFO

Keywords:
Silicide
Crystal structure
Thermoelectric materials
Transport properties
Electrical properties

ABSTRACT

Understanding the structure and its relations with the transport properties is important for designing a good thermoelectric (TE) material. In this work, we investigate the relationship between those properties of the low-cost and eco-friendly materials, β-$Fe_{1-x}Mn_xSi_2$ ($0 \leq x \leq 0.10$), prepared by direct arc melting and heat treatment process. The metallic phases (tetragonal α-Fe_2Si_5 and cubic ε-FeSi) are transformed into the semiconductor phase (orthorhombic β-$FeSi_2$) through heat treatment. The amount of β-$FeSi_2$ significantly decreases at $x \geq 0.09$. Mn atoms act as an acceptor and improve the carrier density (n_H of holes) but decrease the mobility (μ_H). By substituting Mn to β-$FeSi_2$, the Seebeck coefficient (S) is more uniform at high temperatures and the electrical resistivity (ρ) effectively decreases, leading to an improvement in the power factor. The thermal conductivity (κ) slightly increases with Mn doping. However, with increasing Mn content, the formation of secondary phases increases, resulting in the reduction of solid solution of Mn in β-phase; therefore, the electrical transport deteriorates. As a result, the optimum doping level for improving TE performance is obtained at $x = 0.05$ sample, verifying with crystal structure analysis that the optimum doping level is in the range of $0 \leq x \leq 0.08$ because the amount of semiconducting β-$FeSi_2$ drastically drops at $x \geq 0.09$. Our study reveals that by judging the variation of the crystal structures, we could achieve the optimum doping level for improving TE transport properties.

1. Introduction

Thermoelectric (TE) generator is a promising solid-state device to recover waste heat and directly convert it into electrical energy without any moving parts and gas pollution to the environment [1–4]. The efficiency of the TE device is mainly proportional to the performance of TE materials which is called the dimensionless figure of merits (*ZT*). The *ZT* value is theoretically characterized by $ZT = S^2T\rho^{-1}\kappa^{-1}$, where S is the Seebeck coefficient, T is temperature, ρ is electrical resistivity, and κ is the total thermal conductivity contributed by electronic and lattice thermal conductivity ($\kappa = \kappa_e + \kappa_l$). In addition, the term $S^2\rho^{-1}$ is usually called the power factor (*PF*) [5]. Currently, the traditional materials that have acceptable *ZT* values such as lead telluride (PbTe) and bismuth telluride (Bi_2Te_3) alloys are expensive and toxic to the environment [6]. Therefore, researchers attempt to study the properties of abundant and environmentally friendly materials such as Heusler [7–9], sulfide [10, 11], oxides [12–16], and silicide compounds[17–22]. Among silicide compounds, iron silicide (β-$FeSi_2$) is one promising semiconducting material in thermoelectric applications owing to its ability to withstand oxidation and good thermal stability at high temperatures [23–25]. However, the TE performance of pure β-$FeSi_2$ is still limited because of high electrical resistivity (ρ) and the significant reduction of the Seebeck coefficient (S) at high temperatures region. The improvement of S and decrease of ρ can be simultaneously achieved by increasing the carrier density (n_H) to an optimum level. For n-type, the n_H of electrons of β-$FeSi_2$ can be increased by doping elements having more valence electrons at either Fe or Si (for example, doping of Co and Ni at the Fe site) [26–30]. Inversely, for p-type, the n_H of holes can be improved by substituting elements with less valence electrons at either the Fe or Si (for example, doping of Mn or Cr at the Fe site) [31–34].

In the β-$FeSi_2$ system, it was reported the TE performance of the n-type is usually better than the p-type. Ito *et al.* found that the maximum $ZT = 0.25$ of n-type β-$FeSi_2$ is obtained with 5% Co-dopant due to the improvement of the power factor, where the S is uniform and ρ decreased with temperature [35]. Cheng *et al.* have recently reported an improved *ZT* value of 0.3 at 900 K with heavy doping of 8% Co through a long annealing process of 15 days [36]. Qiu *et al.* reported that the heavily Ir-doped β-$FeSi_2$ enhanced the *ZT* value up to 0.6, where Ir acts

* Corresponding author.
E-mail address: nakatsugawa-hiroshi-dx@ynu.ac.jp (H. Nakatsugawa).

https://doi.org/10.1016/j.jallcom.2024.174367
Received 9 February 2024; Received in revised form 23 March 2024; Accepted 31 March 2024

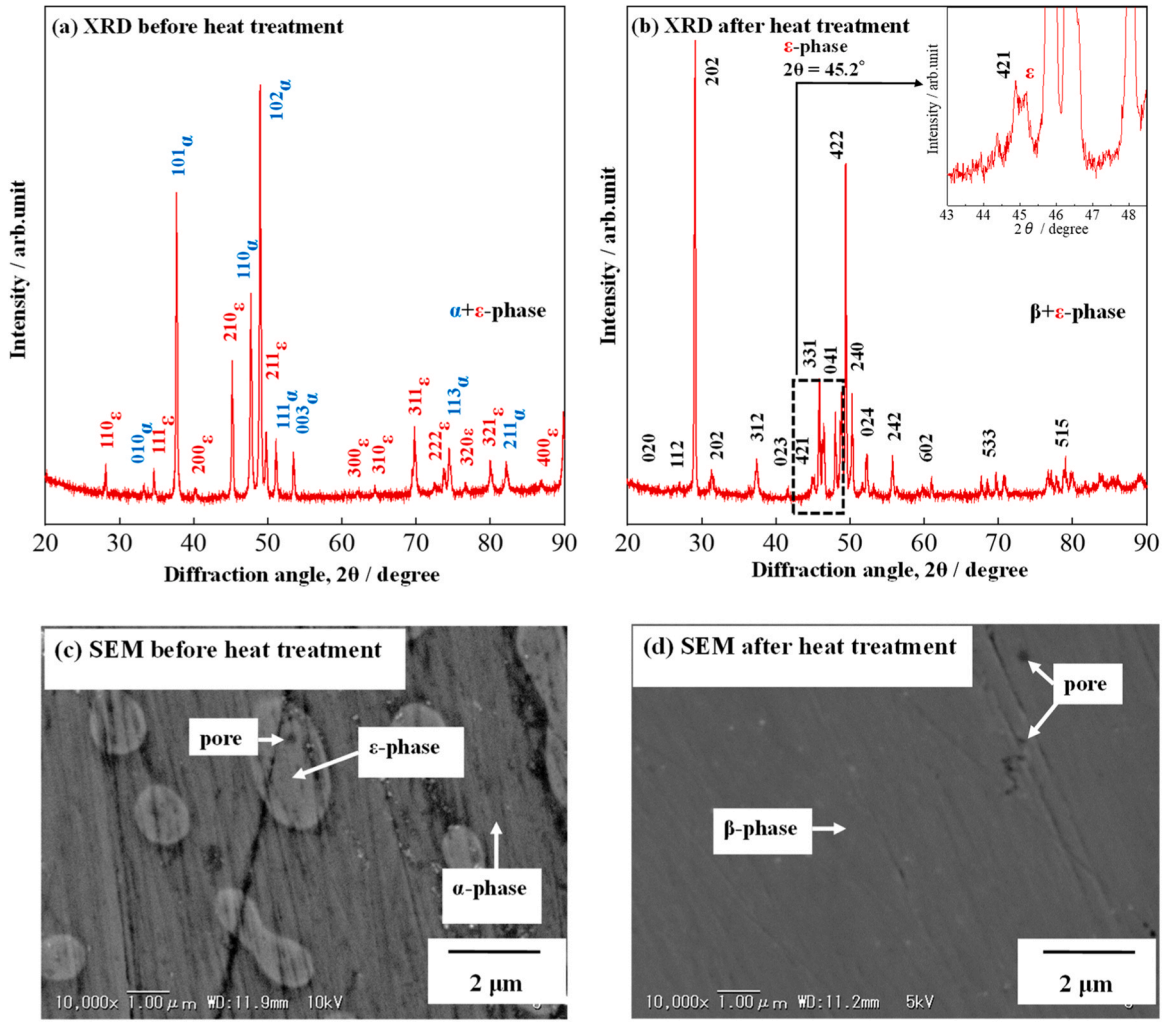

Fig. 1. (a) XRD patterns of $FeSi_2$ before heat treatment, where the indexed peaks are the peak of α and ε-phases. (b) XRD patterns of $FeSi_2$ after heat treatment, where the indexed peaks are the peak of β-phase, and the inset magnifies the peak of ε-phase. (c) SEM image of non-doped $FeSi_2$ before heat treatment and (d) after heat treatment.

not only as a donner to improve the electrical conductivity but also as a heavy element to scatter phonon, resulting in a significant reduction of the thermal conductivity [37]. Du *et al.* reported that the Ru addition to Co-doped β-$FeSi_2$ remarkably reduced thermal conductivity and maximum $ZT = 0.33$ at 900 K was obtained in a 5% Ru-doped sample [38]. Moreover, the Oz substitution on Al-doped β-$FeSi_2$ improved the ZT up to 0.35 because the Oz acts as a heavy element and consequently reduces lattice thermal conductivity [39]. Liu *et al.* reported that the β-$FeSi_2$-SiGe nanocomposite synthesized by the react/transform spark plasma sintering method significantly enhanced electron mobility due to the phase percolation formed by SiGe. As a result, the highest ZT of 0.7 at 973 K was obtained in β-$FeSi_2$-SiGe nanocomposite [40]. Le Tonquesse *et al.* attempted to decrease the thermal conductivity of n-type Co-doped β-$FeSi_2$ by introducing the stacking fault structure, resulting in a 20% reduction in thermal conductivity and an improved ZT of 0.18 at 773 K [28]. Abbassi et *al.* reported that the smallest crystallite sizes of ~50 nm and ~110 nm were obtained in non-doped and 5% Co-doped β-$FeSi_2$ from spark plasma sintering at the optimum conditions pressure of 500 MPa and temperature of 873 K, contributing to the maximum ZT of 0.14 [41]. In addition, we previously reported that the co-doping of Co and Ni on β-$FeSi_2$ prepared by direct arc melting method contributes to the enhancement ZT value of 0.31 at 720 K owing to the improved mobility [20]. On the other hand, other research groups also reported the TE properties of Mn-doped samples synthesized by various methods. Kimura *et al.* reported that the maximum ZT of 0.1 was obtained in a 5% Mn-doped sample synthesized by the gas-atomized powder sintering method [42]. By using vacuum hot-pressing from nitrided rapidly solidified powders, Zhao *et al.* obtained the maximum ZT of 0.17 at 873 K in 8% Mn-doped β-$FeSi_2$, where the fine nitride particles dispersed in β-$FeSi_2$ and enhanced phonon scattering [33]. Yamashita *et al.* prepared a 7% Mn-doped sample by spray drying, compaction, and sintering techniques and reported the highest ZT of 0.15 at 900 K [43]. By employing the pressure sintering method, Ito *et al.* achieved almost the same TE performance ($ZT = 0.14$ at 900 K) [32]. Dabrowski *et al.* reported that the TE p-type β-$FeSi_2$ is much smaller than the n-type. They investigated the TE properties of p-type β-$FeSi_2$ by doping phosphorus (P) to the Si site and manganese (Mn) to the Fe site for the samples fabricated by pulse plasma sintering (PPS) method. For the p-type, the highest ZT value was just about 0.06, obtained with 8% Mn doping [34]. However, there is a lack of understanding of the relationship between structures and transport properties in the β-$FeSi_2$ system. Therefore, we think that it is worth investigating the effect of Mn doping on the structures and electrical transport and finding its optimum doping level to improve the thermoelectric properties of β-$FeSi_2$.

In this work, we investigate in detail the influence of Mn substitution on the variation of crystal structures, microstructures, phase transition, and electrical properties of bulk β-$FeSi_2$ prepared by direct arc melting techniques and followed by a heat treatment process. Importantly, the

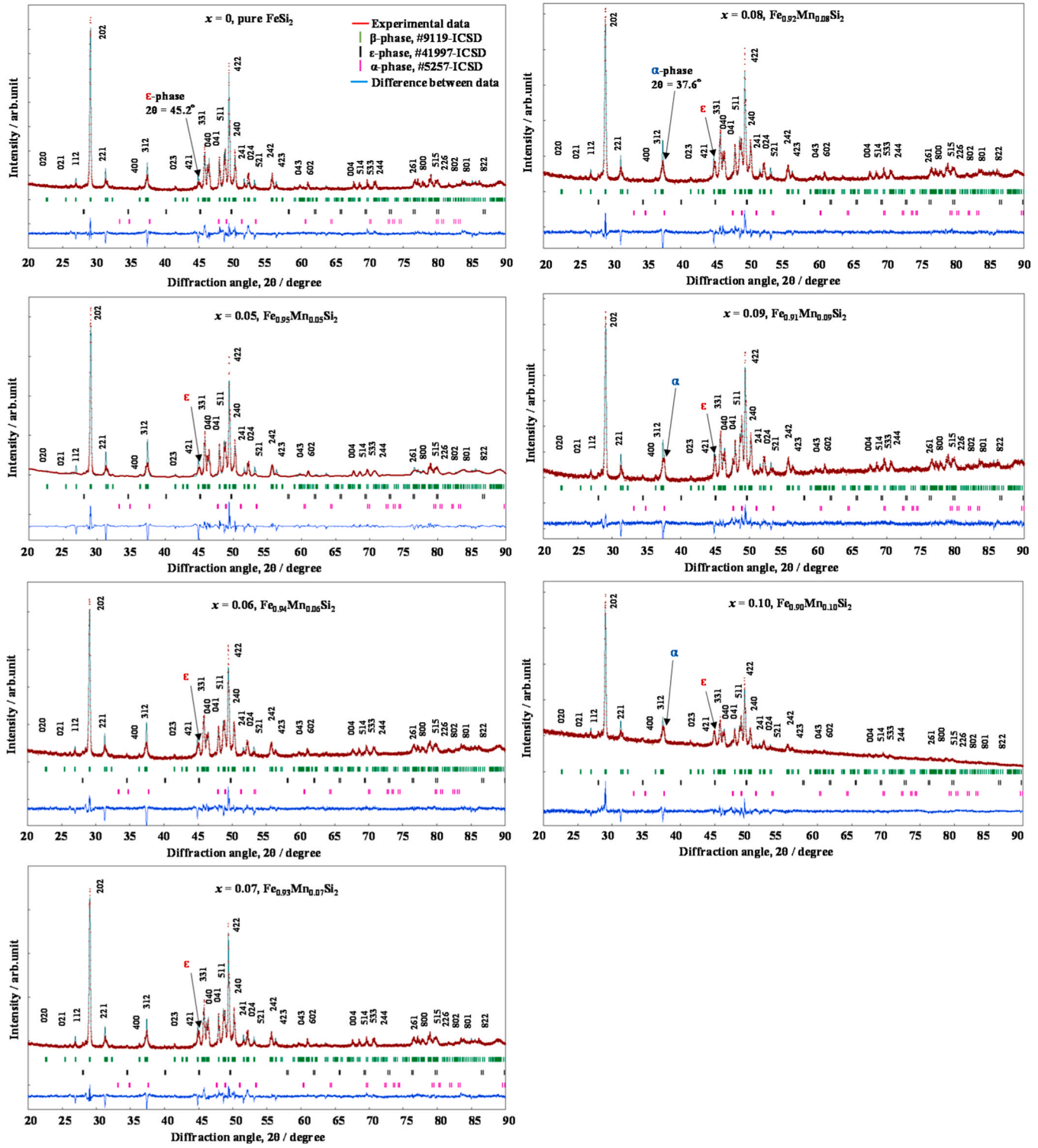

Fig. 2. Rietveld refinement of $Fe_{1-x}Mn_xSi_2$ ($0 \le x \le 0.10$) at diffraction angles of $20° \le 2\theta \le 90°$. The indexed peaks are the peaks of the β-phase. The arrows indicate the variation of the peak intensity of ε and α-phase.

relationship between structures and transport properties is also reported. In addition, we also optimize the Mn doping concentration to improve the thermoelectric properties of p-type β-$Fe_{1-x}Mn_xSi_2$ ($0 \le x \le 0.10$) over the measured temperature from 80 K to 800 K.

2. Experimental methods

2.1. Sample fabrication method

The alloys of bulk β-$Fe_{1-x}Mn_xSi_2$ ($0 \le x \le 0.10$) were prepared by the raw elements of iron (Fe grain, 99.9%), manganese (Mn grain, 99.9%), and silicon (Si grain, 99.999%). Those chemicals were purchased from High Purity Chemical, Japan. The mixtures of raw material were arc

Table 1
Crystal structure parameters of $Fe_{1-x}Mn_xSi_2$ ($0 \leq x \leq 0.10$) at room temperature.

Samples		$Fe_{1-x}Mn_xSi_2$						
Composition, x		0	0.05	0.06	0.07	0.08	0.09	0.10
Space group		*Cmce*	*Cmce*	*Cmce*	*Cmce*	*Cmce*	*Cmce*	*Cmce*
a (Å)		9.8788(5)	9.8780(7)	9.8807(7)	9.8806(3)	9.8769(5)	9.8723(2)	9.8740(8)
b (Å)		7.8008(4)	7.8081(5)	7.8125(6)	7.8136(5)	7.8137(4)	7.8137(2)	7.8162(7)
c (Å)		7.8372(4)	7.8463(6)	7.8497(6)	7.8520(7)	7.8508(4)	7.8471(2)	7.8480(7)
V (Å^3)		603.96(5)	605.18(7)	605.52(4)	606.20(9)	605.88(6)	605.32(3)	605.69(9)
Fe1	x	0.2160(2)	0.2155(2)	0.2157(2)	0.2149(6)	0.2147(2)	0.2135(3)	0.2148(3)
	y	0	0	0	0	0	0	0
	z	0	0	0	0	0	0	0
	B (Å^2)	0.1	0.1	0.1	0.1	0.1	0.1	0.1
	g	1.000	0.950	0.940	0.930	0.920	0.910	0.900
Mn1	x	N/A	0.2155(2)	0.2157(2)	0.2149(6)	0.2147(2)	0.2135(3)	0.2148(8)
	y	N/A	0	0	0	0	0	0
	z	N/A	0	0	0	0	0	0
	B (Å^2)	N/A	0.1	0.1	0.1	0.1	0.1	0.1
	g	N/A	0.050	0.060	0.070	0.080	0.090	0.100
Fe2	x	1/2	1/2	1/2	1/2	1/2	1/2	1/2
	y	0.3014(4)	0.3035(4)	0.3062(4)	0.3065(3)	0.3068(4)	0.3080(5)	0.2982(6)
	z	0.1940(4)	0.1959(4)	0.1925(4)	0.1913(7)	0.1914(3)	0.1864(5)	0.1932(6)
	B (Å^2)	0.1	0.1	0.1	0.1	0.1	0.1	0.1
	g	1.000	0.950	0.940	0.930	0.920	0.910	0.900
Mn2	x	N/A	1/2	1/2	1/2	1/2	1/2	1/2
	y	N/A	0.3035(4)	0.3062(4)	0.3065(3)	0.3068(4)	0.3080(5)	0.2982(6)
	z	N/A	0.1959(4)	0.1925(4)	0.1913(7)	0.1914(3)	0.1864(5)	0.1932(6)
	B (Å^2)	N/A	0.1	0.1	0.1	0.1	0.1	0.1
	g	N/A	0.050	0.060	0.070	0.080	0.090	0.100
Si1	x	0.1217(5)	0.1214(6)	0.1237(6)	0.1229(8)	0.1240(5)	0.1223(6)	0.1160(8)
	y	0.2811(7)	0.2793(6)	0.2769(6)	0.2770(2)	0.2768(6)	0.2778(8)	0.272(1)
	z	0.0394(4)	0.0420(4)	0.0404(4)	0.0405(0)	0.0410(4)	0.0461(6)	0.0469(7)
	B (Å^2)	0.3	0.3	0.3	0.3	0.3	0.3	0.3
	g	1.0	1.0	1.0	1.0	1.0	1.0	1.0
Si2	x	0.3761(5)	0.3778(5)	0.3766(5)	0.3774(5)	0.3775(5)	0.3803(6)	0.3787(7)
	y	0.0399(5)	0.0406(5)	0.0439(5)	0.0433(6)	0.0440(5)	0.0451(6)	0.0630(8)
	z	0.2220(6)	0.2189(6)	0.2223(6)	0.2222(2)	0.2230(6)	0.2181(7)	0.213(1)
	B (Å^2)	0.3	0.3	0.3	0.3	0.3	0.3	0.3
	g	1.0	1.0	1.0	1.0	1.0	1.0	1.0
R_{wp} (%)		3.316	3.001	3.136	3.092	2.826	3.321	3.001
R_P (%)		2.108	1.801	1.923	2.035	1.943	2.291	1.799
R_R (%)		29.041	26.312	26.819	27.501	27.355	34.552	26.289
R_e (%)		0.792	2.161	0.884	1.441	0.824	0.930	2.161
R_B (%)		8.543	7.219	7.368	8.133	8.553	12.343	7.219
R_F (%)		8.603	7.897	5.739	7.066	7.437	8.786	7.882
$S = R_{wp} / R_e$		4.187	1.389	3.549	2.146	3.430	3.571	1.388
Si1 - Fe1 / Mn1 (Å)		2.361(5)	2.381(5)	2.368(6)	2.369(6)	2.363(5)	2.378(7)	2.381(5)
Si1 - Fe1 /Mn1 (Å)		2.402(6)	2.393(6)	2.377(5)	2.387(5)	2.383(5)	2.401(6)	2.393(6)
Si1 - Fe2 / Mn2 (Å)		2.282(5)	2.311(5)	2.294(5)	2.284(5)	2.293(5)	2.289(7)	2.311(6)
Si1 - Fe2 / Mn2 (Å)		2.415(4)	2.387(4)	2.437(4)	2.441(4)	2.442(4)	2.432(6)	2.387(5)
Fe1 / Mn1 - Si1 - Fe1 /Mn1 (deg.)		112.3(2)	112.1(2)	113.3(2)	112.3(1)	113.4(2)	112.4(2)	112.1(2)
Fe2 / Mn2 - Si1 - Fe2 / Mn2 (deg.)		116.6(2)	117.2(2)	116.3(2)	116.8(3)	116.3(2)	117.0(2)	117.1(2)
Si2 - Fe1 / Mn1 (Å)		2.372(5)	2.371(5)	2.386(5)	2.388(5)	2.382(5)	2.378(7)	2.370(5)
Si2 - Fe1 / Mn1 (Å)		2.381(5)	2.411(5)	2.388(5)	2.395(5)	2.402(5)	2.401(6)	2.412(5)
Si2 - Fe2 / Mn2 (Å)		2.322(6)	2.308(6)	2.319(6)	2.313(6)	2.312(6)	2.321(6)	2.308(6)
Si2 - Fe2 /Mn2 (Å)		2.388(5)	2.387(5)	2.395(5)	2.398(5)	2.396(5)	2.382(2)	3.387(4)
Fe1 / Mn1 - Si2 - Fe1 / Mn1 (deg.)		113.5(2)	112.7(2)	113.0(2)	112.8(9)	112.8(1)	111.5(2)	112.6(2)
Fe2 / Mn2 - Si2 - Fe2 /Mn2 (deg.)		116.1(2)	116.5(2)	116.4(2)	116.8(2)	116.9(2)	117.9(2)	116.5(2)

melted in an argon (Ar) atmosphere under low pressure of 10^3 Pa. For such fine-tuned Mn doping, the arc melting process is a critical step. At this step, the Mn element that has the lowest melting point (1519 K), was set at the bottom, and followed by Si and Fe because Si's melting point (1687 K) is lower than Fe (1811 K). It should be noted that the element with the lower melting points needs to be set from the bottom-up. More importantly, to prevent the material from flying out of the copper crucible, the arc power was gradually increased, and the position arc electrode was slowly adjusted during the melting process. It is important to not let the electrode touch the materials. Otherwise, it will contaminate the ingot. Titanium (Ti) with a mass of 10 g was first melted before the main material in order to absorb the residual air inside the melting chamber. The ingots were flipped and remelted three times to ensure the uniformity of the distribution of the materials. After arc melting, the ingot was cut into appropriate smaller pieces (size of 7 mm × 7 mm × 1.5 mm) by using a numerical control wire-discharged cutting machine (Makino, EC-3025). The samples obtained from the arc melting technique are in metallic α+ε-phases that are not preferable for TE application. To transform into semiconducting β-phase, they need to be heat-treated, where the heat treatment condition was optimized by the previous study [44]. The samples were heat-treated in a vacuum-sealed quartz tube at 1423 K for 3 hours and followed by 1113 K for 20 hours. It is noted that the first step of heat treatment is to further homogenize the material distribution and the second step is to transform metal into semiconductor.

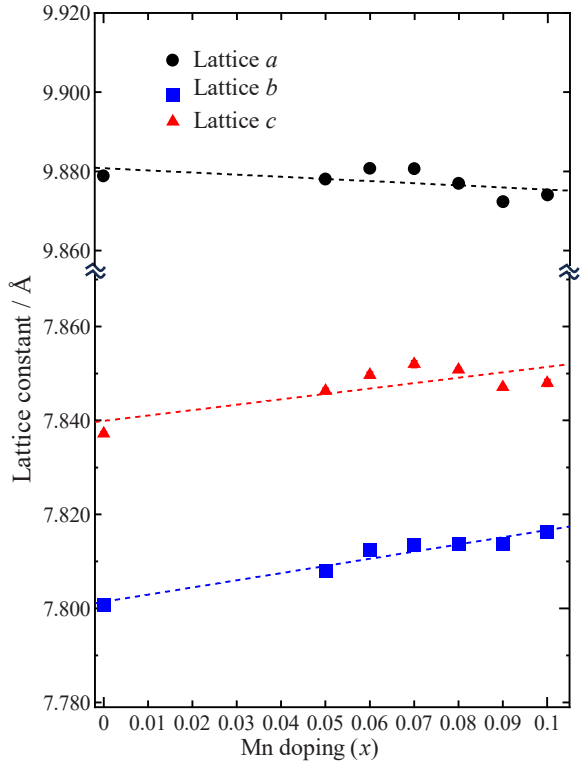

Fig. 3. Lattice constants of $Fe_{1-x}Mn_xSi_2$ ($0 \leq x \leq 0.10$) dependence of Mn doping content.

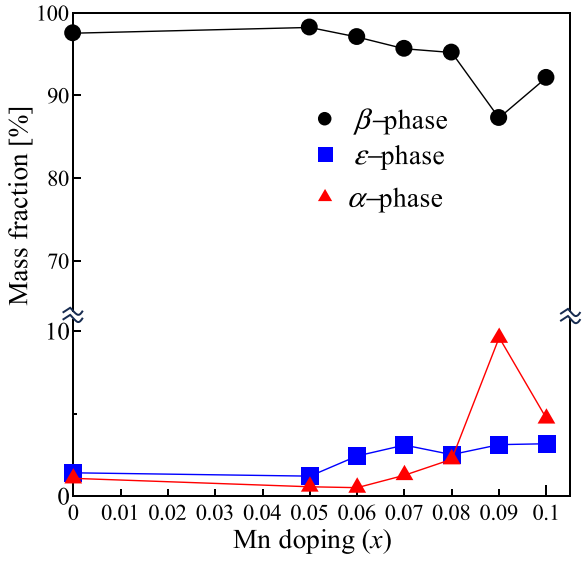

Fig. 4. Phase transition of $Fe_{1-x}Mn_xSi_2$ ($0 \leq x \leq 0.10$) dependence of Mn doping content.

2.2. Characterization methods

The X-ray diffraction (XRD) measurements were conducted by using the X-ray diffractometer equipped with Cu Kα radiation (High-resolution SmartLab, RIGAKU). The phase fraction and crystal structure parameters were computed by the Rietveld refinement method in the RIETAN-FP program, where the occupancy of Fe and Mn was set to 1-*x* and *x*, respectively. The standard crystal data were referred to the Inorganic Crystal Structure Database (ICSD), where code #5257-ICSD was used for α-phase [45], code #41997-ICSD was used for ε-phase [46], and code #9119-ICSD for β-phase [47]. The relative density was measured by a gravity measurement kit (SMK-401, SHIMADZU Co.). The surface morphology was visualized by a scanning electron microscope (SEM, VE8800, KEYENCE). The elemental compositions were characterized by using a scanning electron microscope (SEM, SU8010, Hitachi High-Technologies) equipped with an energy-dispersive X-ray spectroscopy detector (EDS XFlash5060FQ, Bruker). The carrier density (n_H) and mobility (μ_H) were measured at room temperature by the ResiTest8300 apparatus (TOYO Co.). The electrical resistivity (ρ) and Seebeck coefficient (S) were measured by ResiTest8300 apparatus and home-built device from 80 K to 800 K. The thermal conductivity (κ_{total}) was measured by a power efficiency measurement apparatus (PEM-2, ULVAC, Inc.).

Table 2
Elemental composition of $Fe_{1-x}Mn_xSi_2$ measured at room temperature.

x	Area	Element	Atomic %	Composition ratio	Symbol
0.05	β	Fe	35.7(4)	1.07(1)	β-$Fe_{1.07(1)}Mn_{0.051}$
		Mn	1.7(1)	0.051(2)	$_{(2)}Si_{1.88(1)}$
		Si	62.6(5)	1.88(1)	
	ε	Fe	49.4(60	0.98(1)	ε-$Fe_{0.98(1)}Mn_{0.077}$
		Mn	3.8(1)	0.077(2)	$_{(2)}Si_{0.94(1)}$
		Si	46.8(5)	0.94(1)	
0.06	β	Fe	34.1(6)	1.02(1)	β-$Fe_{1.02(1)}Mn_{0.055}$
		Mn	1.8(1)	0.055(2)	$_{(2)}Si_{1.92(1)}$
		Si	64.1(6)	1.92(1)	
	ε	Fe	46.6(8)	0.93(2)	ε-$Fe_{0.93(2)}Mn_{0.091}$
		Mn	4.5(2)	0.091(4)	$_{(4)}Si_{0.98(2)}$
		Si	48.8(9)	0.98(2)	
0.07	β	Fe	33.7(3)	1.01(1)	β-$Fe_{1.01(1)}Mn_{0.058}$
		Mn	1.8(1)	0.058(4)	$_{(4)}Si_{1.93(1)}$
		Si	64.5(5)	1.93(1)	
	ε	Fe	47.1(6)	0.94(1)	ε-$Fe_{0.94(1)}Mn_{0.090}$
		Mn	4.5(2)	0.090(4)	$_{(4)}Si_{0.97(1)}$
		Si	48.4(6)	0.97(1)	
0.08	β	Fe	33.8(5)	1.01(1)	β-$Fe_{1.01(1)}Mn_{0.061}$
		Mn	2.1(1)	0.061(1)	$_{(2)}Si_{1.92(2)}$
		Si	64.1(5)	1.92(2)	
	ε	Fe	46.9(2)	0.94(5)	ε-$Fe_{0.94(5)}Mn_{0.093}$
		Mn	4.7(1)	0.093(2)	$_{(2)}Si_{0.97(4)}$
		Si	48.5(2)	0.97(4)	
0.09	β	Fe	34.2(3)	1.02(1)	β-$Fe_{1.02(1)}Mn_{0.063}$
		Mn	2.1(1)	0.063(1)	$_{(1)}Si_{1.91(1)}$
		Si	63.8(3)	1.91(1)	
	ε	Fe	46.4(6)	0.93(1)	ε-$Fe_{0.93(1)}Mn_{0.099}$
		Mn	4.9(3)	0.099(2)	$_{(2)}Si_{0.97(1)}$
		Si	48.6(3)	0.97(1)	
0.10	β	Fe	33.9(7)	1.02(2)	β-$Fe_{1.02(2)}Mn_{0.049}$
		Mn	1.6(3)	0.049(8)	$_{(8)}Si_{1.93(2)}$
		Si	64.4(6)	1.93(2)	
	ε	Fe	48.5(4)	0.96(1)	ε-$Fe_{0.96(1)}Mn_{0.074}$
		Mn	3.7(4)	0.74(9)	$_{(9)}Si_{0.97(1)}$
		Si	47.3(3)	0.97(1)	

3. Results and discussion

3.1. Crystal structure and microstructures

The XRD data at diffraction angles $20^\circ \leq 2\theta \leq 90^\circ$ and the surface structures of $FeSi_2$ are illustrated in Fig. 1. Before the heat treatment, Fig. 1(a) shows that the sample crystallizes in metallic phases such as α-Fe_2Si_5 (tetragonal structure with *P4/mmm* space group) and ε-FeSi (cubic structure with $P2_13$ space group). After the heat treatment, Fig. 1 (b) indicates that the sample crystallizes in the semiconducting phase, β-$FeSi_2$ (orthorhombic structure with *Cmce* space group), with a trace of ε-phase as shown in the inset. This indicates that heat treatment is important in the Fe-Si system to transform a metal into a semiconducting material which is necessary for TE applications. The SEM image in Fig. 1 (c) confirms that the ε-phase (bright grain) and α-phase (dark grain) are formed after the arc melting. This tendency is consistent with the XRD

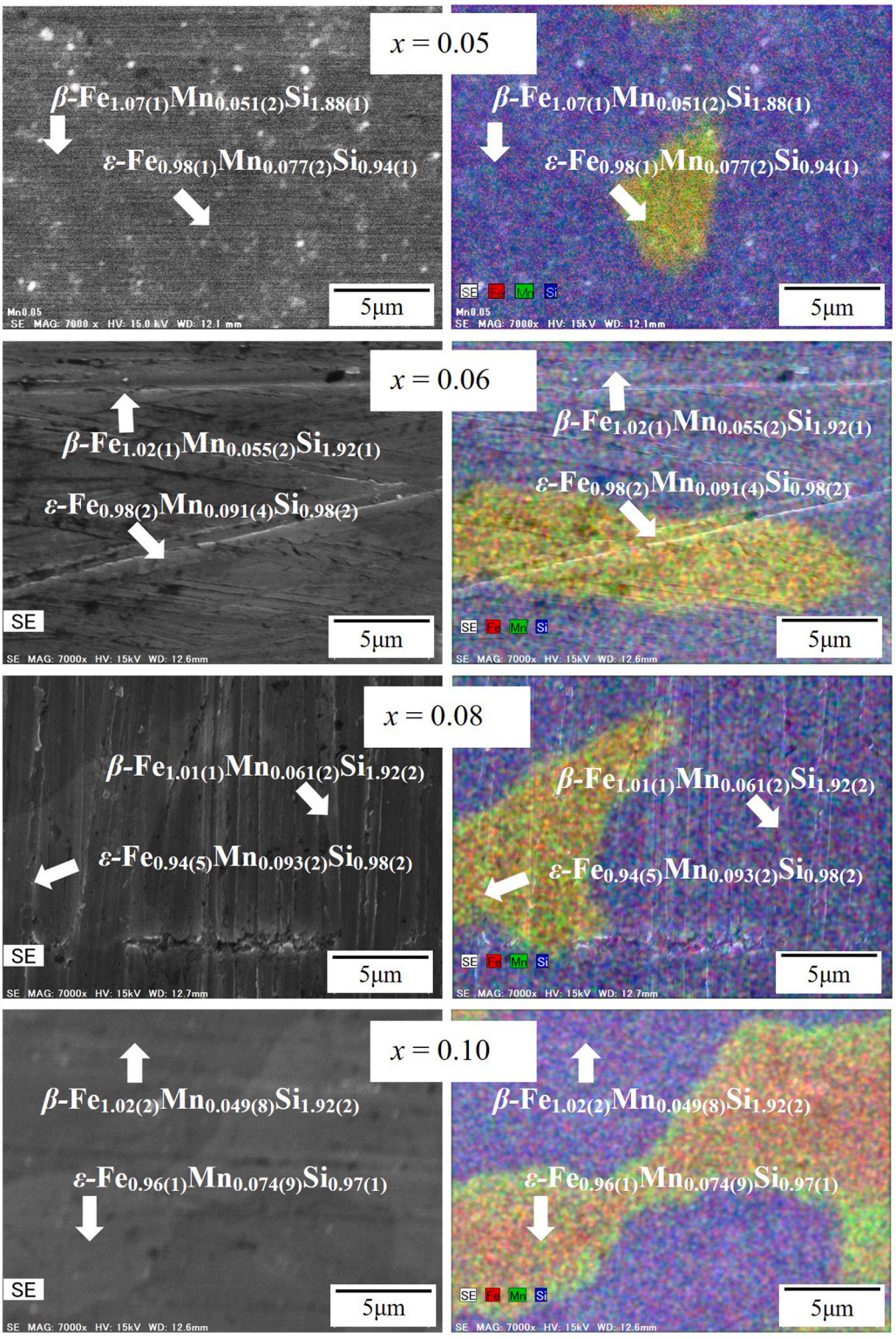

Fig. 5. SEM-EDS mapping of $Fe_{1-x}Mn_xSi_2$, where Fe is mapped in red, Mn in green, and Si in blue. The arrows indicate the area of β-phase and ε-phase.

analysis. In addition, this formation of microstructure is similar to the previous report of Dabrowski et al. [34]. The white dots are not microstructure but just the dust contaminated from the polishing process. It should be noted that the pores are formed which is caused by the rapid cooling of copper heart in the arc melting process. Fig. 1(d) shows that the microstructure is homogeneous in β-$FeSi_2$, verifying with the XRD data in Fig. 1(b). Importantly, the size of pores is enlarged because of the heat treatment process, where the volume of β-phase differs from α and ε-phases (α-Fe_2Si_5 + ε-FeSi ➡ 3β-$FeSi_2$). However, based on the Archimede measurement, the relative density of our samples is higher than 95%. Such a density is comparable to the sample fabricated by the hot pressing method [48] but higher than that prepared by cold-pressed sintering [31], and spark plasma sintering [41,49]. The high relative density could contribute to the improvement in electrical conductivity and performance of TE materials.

The Rietveld refinement of β-$Fe_{1-x}Mn_xSi_2$ ($0 \leq x \leq 0.10$) is shown in

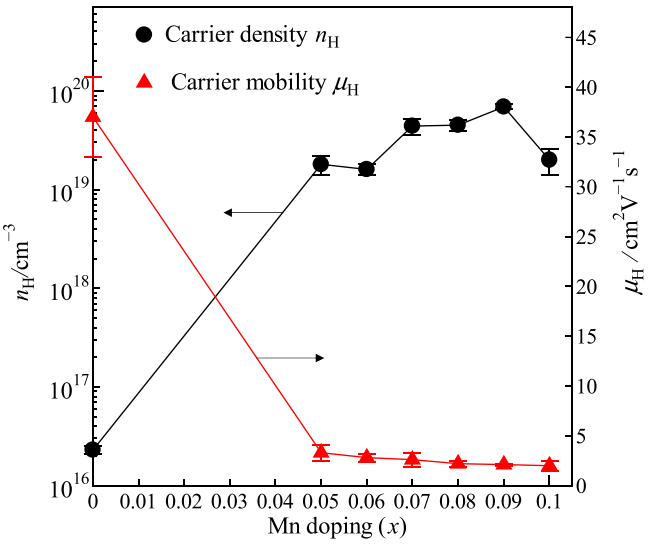

Fig. 6. Carrier density (n_H, on the left axis) and mobility (μ_H, on the right axis) of $Fe_{1-x}Mn_xSi_2$ dependence of Mn doping content at room temperature.

Fig. 2 and the crystal structure parameters are summarized in Table 1. The peak intensity of ε-phase at 2θ = 45.2° of Mn-doped samples is higher than the non-doped sample. The peak of the ε-phase increases with increasing Mn (x) content, indicating that the formation of the secondary phase of β-$FeSi_2$ is so sensitive to dopant. Previous studies also reported that the secondary phase is formed when some dopants such as Cu [32], Ni [20,30], Cr [50], and Co [18,29] are introduced to the β-$FeSi_2$ system. Fig. 3 illustrates the variation of lattice constant with Mn doping. The Mn substitution does not influence lattice constant a but the lattice constant b and c moderately increases with Mn doping. The increase in lattice constants is probably due to the difference in atomic radius, where the Mn radius (r=1.39Å) is larger than that of Fe (r=1.25Å). As a result, the volumes of Mn-doped samples are higher than that of the non-doped sample (Table 1). The addition of some dopants probably does not influence all lattice constants. For example, Kojima *et al.*[51] and Hesse *et al.* [52], pointed out that Co doping increases the lattice constant a, but does not affect the lattice constant b and c. In contrast, our work shows that Mn doping increases lattice constant b and c but does not influence lattice constant a. It is considered that different dopants affect different lattice constants. The Mn atoms should prefer to occupy host atoms orientated along lattice constants b and c.

The quantitative analysis of phase occupation with Mn (x) dependence is plotted in Fig. 4. The amount of β-phase decreases from 97.52% to below 90% as x increases from 0 to 0.10. In contrast, the metallic α + ε-phases significantly increase with Mn content and the α-phase is dominant at $x \geq 0.09$. This tendency suggests that the optimum Mn doping for enhancing TE properties should be in the range of $0 \leq x \leq 0.08$ because the increase in metallic phases could improve the electrical properties but deteriorate the thermopower. Then, we confirm this assumption by studying the TE properties.

The elemental compositions are listed in Table 2. In the area of ε-phase, the Fe:Si ratio is about 1:1, indicating the grain of ε-FeSi. On the other hand, in the area of β-phase, the Fe:Si ratio is approximately 1:2, indicating the β-$FeSi_2$. Fig. 5 shows the SEM-EDS mapping of β-$Fe_{1-x}Mn_xSi_2$. The area of ε-phase increases with increasing x, indicating that Mn contributes to the formation of ε-phase, and it accumulates in those areas as shown in green color. Therefore, it is considered that the formation of ε-phases decreases the solubility of Mn in the β-phase.

Ito *et al.* prepared an 8% Mn-doped β-$FeSi_2$ by employing two different techniques namely hot-pressed and pressureless sintering. Based on the XRD pattern, the presence of ε-phase was confirmed [32]. In addition, Dabrowski *et al.* fabricated an 8% Mn-doped $FeSi_2$ sample by pulse plasma sintering and reported that the ε-phase was also formed based on the XRD peaks and surface morphology analysis [34]. Although the quantitative analysis was not reported, we could assume that Mn was not completely soluble in those samples. In our study, at Mn composition of x = 0.08, the actual x value in the β-phase is approximately 0.061(1) (Table 2). This tendency suggests that the solubility limit of Mn in β-phase is $x \leq 0.06$.

Compared to other metal-doped samples, previous reports found that, based on the XRD patterns, the doping of Cr [50], Cu [32], Ti, Nb, and Zr [53] also provokes the formation of metallic ε-phase. In addition, it was reported that the solubility limit of Co in the β-phase is about 6% [18,54] while that of Ni is about 0.5% [18]. Therefore, the solubility Co in the β-phase is similar to Mn (~6%) as reported by the current study.

3.2. Electrical transport properties

The carrier density (n_H) and mobility (μ_H) of β-$Fe_{1-x}Mn_xSi_2$ ($0 \leq x \leq 0.10$) at room temperature are shown in Fig. 6. The n_H of Mn-doped samples (~10^{19} cm^{-3}) is three orders of magnitude higher than the non-doped sample (~10^{16} cm^{-3}), indicating that the electrical conductivity is improved by Mn substitution. However, the n_H slightly decreases at $x \geq 0.09$ due to the decrease in solubility of Mn in β-$FeSi_2$ as discussed above in elemental analysis and SEM-EDS mapping. As shown in Table 3, the sign of the Seebeck coefficient of the non-doped sample is negative (-) but that of Mn-doped samples is positive (+). This tendency suggests that Mn acts as an acceptor in the β-$FeSi_2$ system. The μ_H of the Mn-doped sample is smaller than that of the Mn-doped sample probably due to the increase in scattering frequency when more carriers are introduced to the β-$FeSi_2$. The decrease in μ_H could contribute to the enhancement of the Seebeck coefficient and consequently improve TE performance. For Mn doping, the μ_H of our samples (2–3 cm^{2}V^{-1}s^{-1}) is slightly smaller than that fabricated by the cold-pressed sintering method (3–7 cm^{2}V^{-1}s^{-1}) as reported by Tani et al. [31] but the n_H is about one order of magnitude higher. This is probably due to the lower density because the relative density of the cold-pressed sintering sample is only about 80% while our sample is higher than 95%.

3.3. Thermoelectric properties

Fig. 7 shows the temperature dependence of electrical resistivity (ρ), Seebeck coefficient (S), n_H versus $|S|$, and power factor (PF). The ρ of all Mn-doped samples is remarkably smaller than the non-doped sample

Table 3
Summary of thermoelectric properties of $Fe_{1-x}Mn_xSi_2$ ($0 \leq x \leq 0.10$) at room temperature, where L_0, $r = -1/2$, n_H, μ_H, S, ρ, and κ are Lorenz number, scattering factor (for acoustic phonon scattering), carrier density, mobility, Seebeck coefficient, electrical resistivity, and total thermal conductivity, respectively.

x	L_0 [V^{2}K^{-2}]	r	n_H [cm^{-3}]	μ_H [cm^{2}V^{-1}s^{-1}]	S [μVK^{-1}]	ρ [Ωcm]	κ [Wm^{-1}K^{-1}]
0	1.792×10^{-8}	−1/2	$2.3(2) \times 10^{16}$	37(4)	-127	7.10	7.67
0.05	1.631×10^{-8}	−1/2	$1.8(4) \times 10^{19}$	3.3(8)	254	0.10	7.20
0.06	1.628×10^{-8}	−1/2	$1.6(2) \times 10^{19}$	2.8(4)	279	0.14	8.61
0.07	1.656×10^{-8}	−1/2	$4.4(8) \times 10^{19}$	2.6(7)	194	0.05	6.99
0.08	1.663×10^{-8}	−1/2	$4.5(6) \times 10^{19}$	2.2(3)	186	0.05	6.89
0.09	1.715×10^{-8}	−1/2	$6.9(4) \times 10^{19}$	2.1(1)	153	0.04	8.03
0.10	1.711×10^{-8}	−1/2	$2.0(6) \times 10^{19}$	2.0(5)	155	0.16	7.66

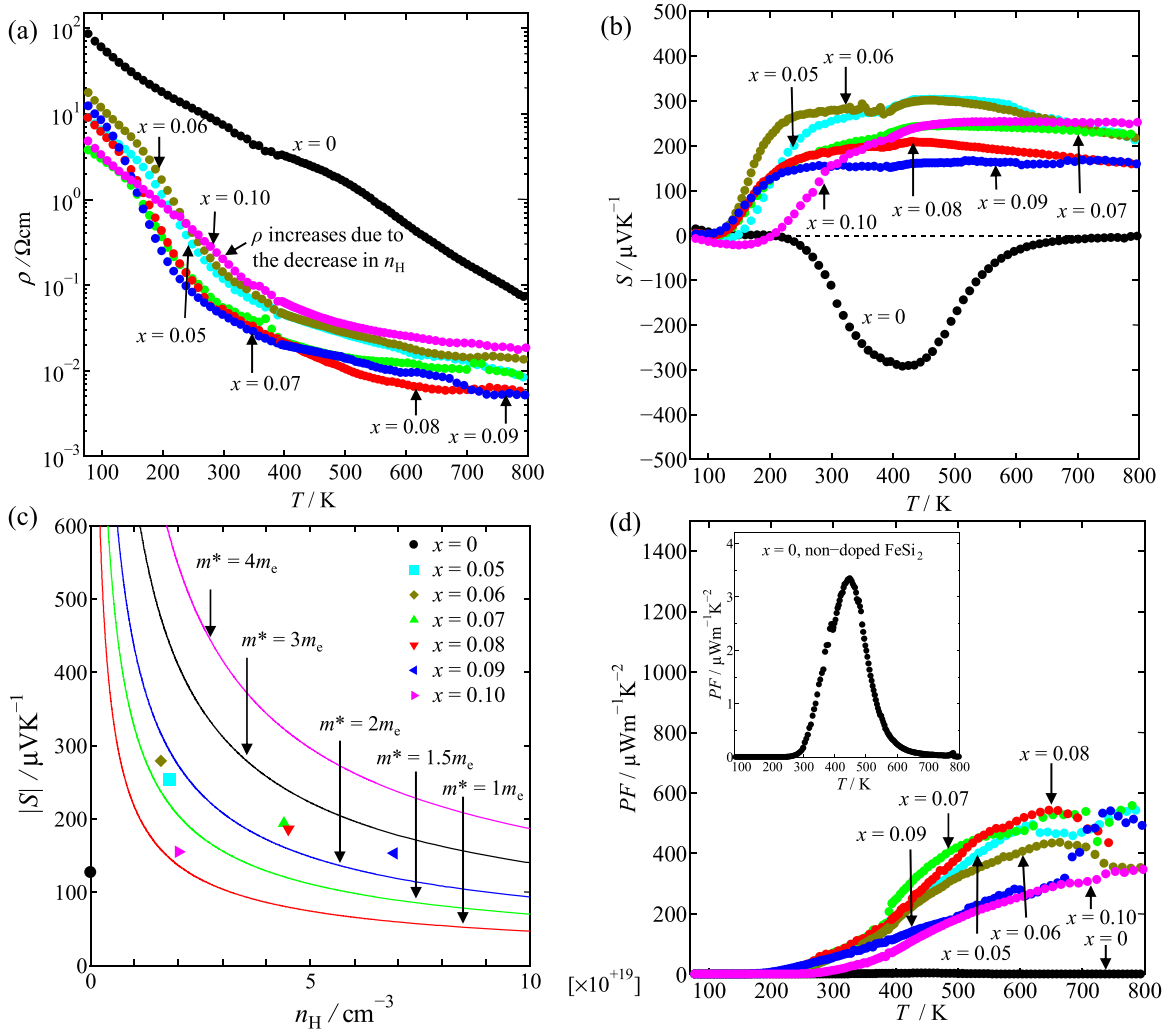

Fig. 7. Temperature dependence of (a) electrical resistivity, ρ, and (b) Seebeck coefficient, S, of $Fe_{1-x}Mn_xSi_2$ ($0 \le x \le 0.10$). (c) Absolute Seebeck coefficient, $|S|$, versus carrier density, n_H at room temperature, and the solid lines are the calculated data by using Mott's equation at various effective masses ($m^* = xm_e$, where x is variable and m_e is the static mass of the electron, i.e., 9.10938×10^{-31} kg. (d) Temperature dependence of power factor and inset magnified the data of the non-doped sample.

over measured temperatures from 80 to 800 K, especially since it is two orders of magnitude smaller (~10^{-2} Ωcm) at high temperatures (Fig. 7 (a)). The decrease in ρ is due to the increase in n_H as can be expressed by Drude's theory:

$$\rho = \frac{1}{|e|\mu_H n_H} \tag{1}$$

Here, e is elementary change, μ_H is mobility, and n_H is carrier density [55]. The Eq. (1) indicates that the n_H is inversely proportional to ρ. In addition, the ρ of all samples decreases with temperature, suggesting that more carriers are excited as temperature increases.

In Fig. 7(b), for the $x = 0$ sample, at the temperature region below 420 K, the $|S|$ increases with increasing temperature because of the transition from impurity band conduction to polaron conduction [39, 56]. At above 420 K, it was argued that due to the semiconductor-to-metal transition, $|S|$ decreases with increasing temperature [56]. However, as it is clear from Fig. 7(a), the x=0 sample shows no metal-insulator transition at 420 K. It shows semiconducting behavior over the entire temperature range. Therefore, the decrease of $|S|$ at high temperatures is not due to semiconductor-to-metal transition, but it should be due to the bipolar effect that usually happens in intrinsic semiconductors. On the other hand, the S of Mn-doped samples is more uniform over 300–800 K probably due to the increase in scattering frequency when n_H increases. In addition, there are some transitions from n-type to p-type semiconductor as the temperature changes. For example, the sign of S of $x = 0.10$ sample changes from negative (-) to positive (+) at 200 K. This indicates that more holes are excited with increasing temperature. The conduction is dominated by both electrons and holes, where their ratio varies with temperatures [26]. In addition, the S decreases with increasing x due to the increase in n_H as explained by Mott's theory:

$$|S| = \frac{k_B^2 T}{3|e|\hbar^2} m^* \left(\frac{\pi}{3n_H}\right)^{2/3} \tag{2}$$

where $|S|$ is the absolute Seebeck coefficient, k_B is Boltzmann constant, T is temperature, $\hbar$ is Plack constant, e is elementary charge m^* is effective mass, and n_H is carrier concentration [57]. The Eq. (2) indicates that when increasing n_H, the $|S|$ will decrease. If we plot $|S|$ versus n_H of experimental data and calculated value by using Mott's formula, a good fitting is obtained at the effective mass of $m^* = 2m_e$, where m_e is the static mass of the electron, i.e., 9.10938×10^{-31} kg (Fig. 7(c)).

The power factor ($PF = S^2/\rho$) with temperature dependence is illustrated in Fig. 7(d). As shown in the inset, the maximum PF value of the non-doped sample is very small (3.4 $\mu Wm^{-1}K^{-2}$ at 450 K) while the value of all Mn-doped samples is higher than 250 $\mu Wm^{-1}K^{-2}$ at 800 K.

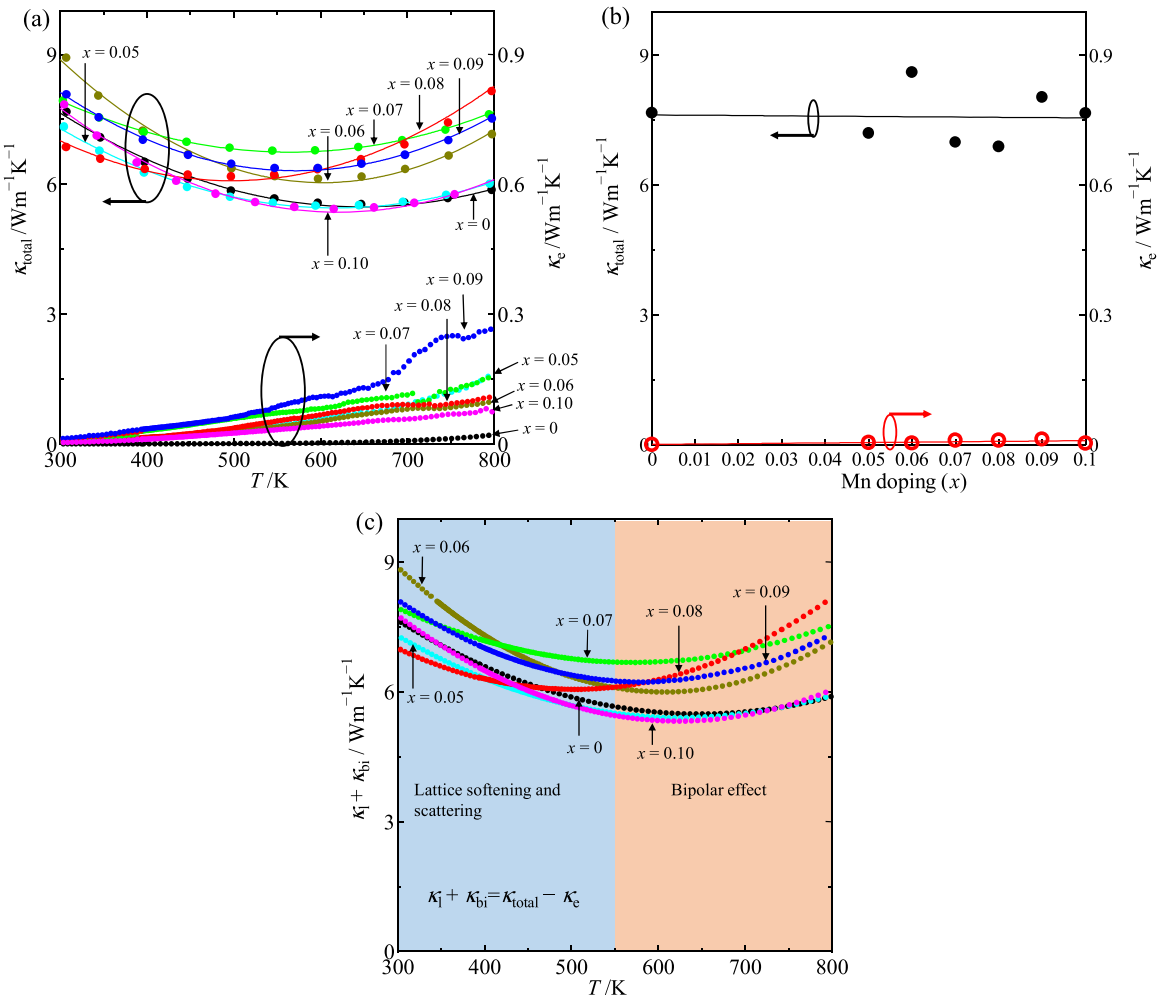

Fig. 8. (a) Temperature dependence of total thermal conductivity, k_{total}, (left axis) and electronic thermal conductivity, k_e, (right axis) of $Fe_{1-x}Mn_xSi_2$ ($0 \le x \le 0.10$), and (b) the thermal conductivity dependence with Mn doping content at room temperature. The black solid circles are the data of k_{total} (left axis) and the open red circles are the data of k_e (right axis). The straight lines are the approximation lines for each data. (d) Temperature dependence of lattice thermal conductivity and bipolar thermal conductivity ($k_l + k_{bi}$). The lattice softening and scattering contribute at low temperatures as highlighted in the shaded blue region while bipolar effect contributes at higher temperatures highlighted in the shaded orange region.

The improved *PF* values are contributed by the decreased ρ and uniform *S* at high temperatures. The highest *PF* value of about 530 $\mu Wm^{-1}K^{-2}$ at 650 K is obtained in the $x = 0.08$ sample and almost the same value is in the $x = 0.05$ sample at 800 K. At room temperature, the *PF* value of our sample (70 $\mu Wm^{-1}K^{-2}$) is greater than that of the thin film sample (2.4 $\mu Wm^{-1}K^{-2}$) prepared by the radio frequency sputtering method [58].

The temperature-dependent thermal conductivity is shown in Fig. 8 (a). The total thermal conductivity (κ_{total}) is plotted on the left side and electronic thermal conductivity (κ_e) is plotted on the right side. The κ_{total} slightly increases with *x* due to the formation of metallic ε+α-phase as discussed in structural analysis in the above section. In addition, the increase of κ_e also contributes to the increase of κ_{total} ($\kappa_e + \kappa_l = \kappa_{total}$, where κ_l is the lattice thermal conductivity). The κ_e is calculated by Wiedemann–Franz law: $\kappa_e = L_0\rho^{-1}T$, where L_0 is the Lorenz number, ρ is electrical resistivity, and *T* is temperature. In the case of acoustic scattering with the scattering factor of $r = -1/2$, the L_0 can be calculated by using experimental values of the Seebeck coefficient (*S*). The relationship between *r* and L_0 is expressed by:

$$L_0 = \left(\frac{k_B}{e}\right)^2 \left[\frac{\left(r+\frac{7}{2}\right)F_{r+\frac{5}{2}}(\eta)}{\left(r+\frac{3}{2}\right)F_{r+\frac{1}{2}}(\eta)} - \left\{\frac{\left(r+\frac{5}{2}\right)F_{r+\frac{3}{2}}(\eta)}{\left(r+\frac{3}{2}\right)F_{r+\frac{1}{2}}(\eta)}\right\}^2\right] \quad (3)$$

where the function is: $F_n(\eta) = \int_0^\infty \frac{\chi^n}{1+e^{\chi-\eta}}d\chi$, $\chi = \frac{E}{k_BT}$, $\eta = \frac{E_F}{k_BT}$. The E_F is the Fermi energy [59]. The calculated values of L_0 are listed in Table 3. The L_0 increases as *x* increases from 0.05 to 0.10, suggesting that the semiconducting β-phase transforms to metallic phase ε+α-phase. Fig. 8 (b) shows the room temperature data of total thermal conductivity and electronic thermal conductivity with *x* dependence. If we compare the ratio between electronic thermal conductivity and the total thermal conductivity, the values of electronic thermal conductivity are very small and negligible ($\kappa_e << \kappa_l$), indicating the lattice thermal conductivity is dominant to the total thermal conductivity. This suggests that the Mn atoms have extra phonon scattering contribution that affects the lattice thermal conductivity. The lattice thermal conductivity κ_l has relations with the specific heat at constant volume (C_v), phonon group velocity (v_G), and relaxation time (τ) or phonon mean free path (ℓ) as expressed by the following formula [55]:

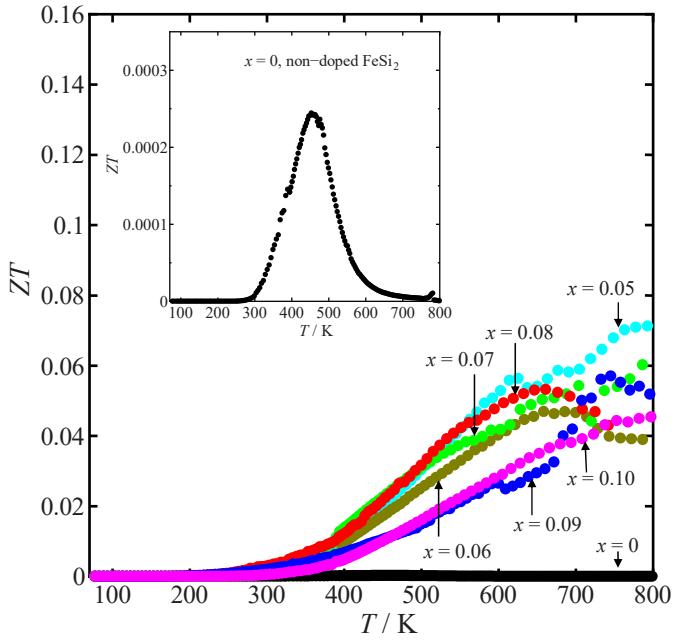

Fig. 9. Temperature dependence of ZT values of $Fe_{1-x}Mn_xSi_2$ ($0 \le x \le 0.10$), where the inset magnified the data of the non-doped sample.

$$\kappa_l = (1/3)C_v\nu_G^2\tau = (1/3)C_v\nu_G\ell \quad (4)$$

In Eq. (4), ℓ is equal to $\nu_G\tau$. The κ_l is mainly influenced by ν_G and τ or ℓ. Fig. 8(c) shows temperature dependence lattice thermal conductivity and bipolar thermal conductivity ($k_l + k_{bi}$) and two regions are observed. In the first region, at low temperatures, the thermal conductivity decreases with increasing temperature due to lattice softening and phonon scattering [60,61]. It should be noted that when dopant (Mn) atoms occupy host atoms ($FeSi_2$), the internal strain field of the system increases. Thus, it changes the phonon frequency locally and induces both lattice softening and phonon scattering. Lattice softening decreases the phonon speed (ν_G) while phonon scattering decreases relaxation time (τ) or mean free path (ℓ). Therefore, the decrease in thermal conductivity could be possibly caused by both lattice softening (slow phonon velocity) and lattice scattering (short mean free path). In the second region, at higher temperatures, due to the extra contribution of the bipolar effect [60,62,63], the thermal conductivity increases with increasing temperature.

The TE performance, $ZT = S^2T\rho^{-1}\kappa^{-1}$, with temperature dependence is shown in Fig. 9 and the inset magnified the data of the non-doped sample. The inset shows that the maximum ZT value of the $x = 0$ sample is about 2.4×10^{-4} at 450 K. Such a value is much smaller than that of all Mn-doped samples. The highest $ZT = 0.07$ at 800 K is obtained $x = 0.05$ because of the improvement in PF values, where ρ is reduced and S is enhanced. It is confirmed with the crystal structure analysis that the optimum doping is in the range of $0 \le x \le 0.08$ because the metallic α-Fe_2Si_5 is dominant at $x \ge 0.09$. The ZT value of the current study is lower than the Mn-doped samples prepared by the gas-atomized powder sintering method (ZT=0.1) [42], hot pressing and rapid solidification (ZT=0.17) [33], spray drying and sintering techniques (ZT=0.15) [43], and pressure sintering method (ZT=0.14) [32]. However, it is comparable to the sample prepared by pulse plasma sintering [34] and much higher than Cr and Zr-doped $FeSi_2$ [8,50]. The proposed direct arc melting technique of our study is more convenient for producing TE materials. The future study is worth investigating the strategy to reduce the thermal conductivity of $x = 0.08$ sample by alloying with heavy elements such as ruthenium (Ru) or germanium (Ge).

4. Conclusions

β-$Fe_{1-x}Mn_xSi_2$ ($0 \le x \le 0.10$) samples were successfully fabricated by direct arc melting and heat treatment. By investigating the transition in the crystal structure, we obtain the optimum Mn doping range of $0 \le x \le 0.08$ for enhancing the transport properties. The metallic phases (α-Fe_2Si_5 and ε-FeSi) increase with increasing Mn doping, resulting in a decrease in the solid solution of Mn in β-$FeSi_2$. Mn plays a role as an acceptor in β-$FeSi_2$ and improves carrier density (n_H). The increase in n_H improves electrical conductivity and uniform Seebeck coefficient at high-temperature regions. The thermal conductivity slightly increases with x due to the formation of the metallic phase. The highest thermoelectric performance is obtained in the $x = 0.05$ sample verified with crystal structure analysis. This study establishes a strategy to correlate the structural and transport properties in transition metal silicides to achieve the optimum doping level for enhancing transport performance.

CRediT authorship contribution statement

Mizuki Namba: Data curation. **Kosuke Yamazaki:** Methodology. **Sopheap Sam:** Writing – review & editing, Writing – original draft, Visualization, Methodology, Investigation, Formal analysis, Data curation, Conceptualization. **Umar Farooq:** Data curation. **Hiroshi Nakatsugawa:** Writing – review & editing, Supervision, Software, Resources, Project administration, Funding acquisition.

Declaration of Competing Interest

The authors declare that they have no known competing financial interests or personal relationships that could have appeared to influence the work reported in this paper.

Data Availability

Data will be made available on request.

Acknowledgments

The XRD and SEM-EDS measurements were performed at the Instrumental Analysis and Evaluation Center, Yokohama National University. The thermal conductivity was measured by the PEM-2 apparatus at National Defense Academy.

References

[1] H. Jouhara, N. Khordehgah, S. Almahmoud, B. Delpech, A. Chauhan, S.A. Tassou, Therm. Sci. Eng. Prog. 6 (2018) 268–289, https://doi.org/10.1016/j.tsep.2018.04.017.
[2] S. Sam, L.A. Gan Lim, S. Thirumalai, A. Wiranata, Jamasri, J. Sentanuhady, G.N. C. Santos, M.A. Muflikhun, Manuf. Lett. 40 (2024) 11–15, https://doi.org/10.1016/j.mfglet.2024.01.002.
[3] Fitriani, R. Ovik, B.D. Long, M.C. Barma, M. Riaz, M.F.M. Sabri, S.M. Said, R. Saidur, Renew. Sustain. Energy Rev. 64 (2016) 635–659, https://doi.org/10.1016/j.rser.2016.06.035.
[4] G. Latronico, P. Mele, C. Sekine, P.S. Wei, S. Singh, T. Takeuchi, C. Bourgès, T. Baba, T. Mori, P. Manfrinetti, C. Artini, Nanotechnology 34 (2023), https://doi.org/10.1088/1361-6528/aca980.
[5] H.J. Goldsmid, Theory of Thermoelectric Refrigeration and Generation, in: H. Robert, J. Chennupati, K. Yoshiyuki, M.O. Richard, P. Jürgen, S. Tae-Yeon, U. Shin-ichi, M.W. Zhiming (Eds.), Intoduction to Thermoelectr., 2nd ed., Springer Berlin Heidelberg, Berlin, Heidelberg, 2016, pp. 9–24, https://doi.org/10.1007/978-3-662-49256-7_2.
[6] X.F. Zheng, C.X. Liu, Y.Y. Yan, Q. Wang, Renew. Sustain. Energy Rev. 32 (2014) 486–503, https://doi.org/10.1016/j.rser.2013.12.053.
[7] H. Nakatsugawa, T. Ozaki, H. Kishimura, Y. Okamoto, J. Electron. Mater. 49 (2020) 2802–2812, https://doi.org/10.1007/s11664-019-07855-7.
[8] S. Katsuyama, H. Matsushima, M. Ito, J. Alloy. Compd. 385 (2004) 232–237, https://doi.org/10.1016/j.jallcom.2004.02.061.
[9] A. Difalco, I.G. Winning, M. Palumbo, M. Baricco, A. Castellero, E. Alleno, Solid State Sci. 149 (2024) 107455, https://doi.org/10.1016/j.solidstatesciences.2024.107455.

[10] X. Chen, H. Zhang, Y. Zhao, W.-D. Liu, W. Dai, T. Wu, X. Lu, C. Wu, W. Luo, Y. Fan, L. Wang, W. Jiang, Z.-G. Chen, J. Yang, ACS Appl. Mater. Interfaces 11 (2019) 22457–22463, https://doi.org/10.1021/acsami.9b06212.
[11] X.-Q. Chen, S.-J. Fan, C. Han, T. Wu, L.-J. Wang, W. Jiang, W. Dai, J.-P. Yang, Rare Met 40 (2021) 2017–2025, https://doi.org/10.1007/s12598-020-01698-6.
[12] H. Nakatsugawa, M. Kubota, M. Saito, J. Jpn. Inst. Met. 79 (2015) 597–606, https://doi.org/10.2320/jinstmet.JA201516.
[13] H. Fukutomi, Y. Konno, K. Okayasu, M. Hasegawa, H. Nakatsugawa, Mater. Sci. Eng. A 527 (2009) 61–64, https://doi.org/10.1016/j.msea.2009.08.012.
[14] H. Nakatsugawa, M. Saito, Y. Okamoto, J. Electron. Mater. 46 (2017) 3262–3272, https://doi.org/10.1007/s11664-017-5366-3.
[15] H. Nakatsugawa, M. Saito, Y. Okamoto, Mater. Trans. 60 (2019) 1051–1060, https://doi.org/10.2320/matertrans.E-M2019812.
[16] H. Nakatsugawa, Y. Kamatani, Y. Okamoto, C.H. Hervoches, Jpn. J. Appl. Phys. 62 (2023) 043001, https://doi.org/10.35848/1347-4065/acc9f3.
[17] A.T. Burkov, Phys. Status Solidi 215 (2018) 1800105, https://doi.org/10.1002/pssa.201800105.
[18] S. Sam, K. Yamazaki, H. Nakatsugawa, Solid State Commun. 371 (2023) 115287, https://doi.org/10.1016/j.ssc.2023.115287.
[19] A. Binti Abdullah Zaik, F. Liana Binti Mohd. Redzuan, S. Ahmad Zaki Bin Shaikh Salim, A. Faiz Bin Mohammad, M. Fitri Bin Mohd. Yakub, M. Takeda, Mater. Today Proc. 65 (2022) 2979–2985, https://doi.org/10.1016/j.matpr.2022.03.150.
[20] S. Sam, H. Nakatsugawa, Y. Okamoto, Mater. Adv. 4 (2023) 2821–2830, https://doi.org/10.1039/D3MA00153A.
[21] A. Nozariasbmarz, A. Agarwal, Z.A. Coutant, M.J. Hall, J. Liu, R. Liu, A. Malhotra, P. Norouzzadeh, M.C. Öztürk, V.P. Ramesh, Y. Sargolzaeiaval, F. Suarez, D. Vashaee, Jpn. J. Appl. Phys. 56 (2017) 05DA04, https://doi.org/10.7567/JJAP.56.05DA04.
[22] F.L.B.M. Redzuan, I. Mikio, T. Masatoshi, J. Mater. Sci. 53 (2018) 7683–7690, https://doi.org/10.1007/s10853-018-2066-1.
[23] T. Kojima, Phys. Status Solidi 111 (1989) 233–242, https://doi.org/10.1002/pssa.2211110124.
[24] U. Stöhrer, R. Voggesberger, G. Wagner, U. Birkholz, Energy Convers. Manag. 30 (1990) 143–147, https://doi.org/10.1016/0196-8904(90)90025-T.
[25] H. Inoue, T. Kobayashi, M. Kato, S. Yoneda, J. Electron. Mater. 45 (2016) 1767–1771, https://doi.org/10.1007/s11664-015-4208-4.
[26] J. Tani, H. Kido, J. Appl. Phys. 84 (1998) 1408–1411, https://doi.org/10.1063/1.368174.
[27] Z. He, D. Platzek, C. Stiewe, H. Chen, G. Karpinski, E. Müller, J. Alloy. Compd. 438 (2007) 303–309, https://doi.org/10.1016/j.jallcom.2006.08.045.
[28] S. Le Tonquesse, Z. Verastegui, H. Huynh, V. Dorcet, Q. Guo, V. Demange, C. Prestipino, D. Berthebaud, T. Mori, M. Pasturel, ACS Appl. Energy Mater. 2 (2019) 8525–8534, https://doi.org/10.1021/acsaem.9b01426.
[29] S. Sam, H. Nakatsugawa, Y. Okamoto, Jpn. J. Appl. Phys. 61 (2022) 111002, https://doi.org/10.35848/1347-4065/ac96b7.
[30] S. Sam, S. Odagawa, H. Nakatsugawa, Y. Okamoto, Materials (Basel) 16 (2023) 927, https://doi.org/10.3390/ma16030927.
[31] J. Tani, H. Kido, J. Appl. Phys. 86 (1999) 464–467, https://doi.org/10.1063/1.370753.
[32] M. Ito, H. Nagai, T. Tanaka, S. Katsuyama, K. Majima, J. Alloy. Compd. 319 (2001) 303–311, https://doi.org/10.1016/S0925-8388(01)00920-3.
[33] X.B. Zhao, H.Y. Chen, E. Müller, C. Drasar, Appl. Phys. A 80 (2005) 1123–1127, https://doi.org/10.1007/s00339-004-2596-z.
[34] F. Dąbrowski, Ł. Ciupiński, J. Zdunek, J. Kruszewski, R. Zybała, A. Michalski, K. Jan Kurzydłowski, Mater. Today Proc. 8 (2019) 531–539, https://doi.org/10.1016/j.matpr.2019.02.050.
[35] J. Tani, H. Kido, Jpn. J. Appl. Phys. 40 (2001) 3236, https://doi.org/10.1143/JJAP.40.3236.
[36] J. Cheng, L. Gan, J. Zhang, J. Xi, L. Xi, J. Yang, T. Deng, P. Qiu, X. Shi, L. Chen, J. Mater. Sci. Technol. 187 (2024) 248–257, https://doi.org/10.1016/j.jmst.2023.11.039.
[37] P. Qiu, J. Cheng, J. Chai, X. Du, X. Xia, C. Ming, C. Zhu, J. Yang, Y. Sun, F. Xu, X. Shi, L. Chen, Adv. Energy Mater. 12 (2022) 2200247, https://doi.org/10.1002/aenm.202200247.
[38] X. Du, P. Hu, T. Mao, Q. Song, P. Qiu, X. Shi, L. Chen, ACS Appl. Mater. Interfaces 11 (2019) 32151–32158, https://doi.org/10.1021/acsami.9b10648.
[39] X. Du, P. Qiu, J. Chai, T. Mao, P. Hu, J. Yang, Y.-Y. Sun, X. Shi, L. Chen, ACS Appl. Mater. Interfaces 12 (2020) 12901–12909, https://doi.org/10.1021/acsami.0c00321.
[40] N. Liu, S.E. Rezaei, W.A. Jensen, S. Song, Z. Ren, K. Esfarjani, M. Zebarjadi, J. A. Floro, Adv. Funct. Mater. 29 (2019) 1903157, https://doi.org/10.1002/adfm.201903157.
[41] L. Abbassi, D. Mesguich, D. Berthebaud, S. Le Tonquesse, B. Srinivasan, T. Mori, L. Coulomb, G. Chevallier, C. Estournès, E. Flahaut, R. Viennois, M. Beaudhuin, Nanomaterials 11 (2021) 2852, https://doi.org/10.3390/nano11112852.
[42] Y. Kimura, M. Yamada, Y.W. Chai, Mater. Trans. 60 (2019) 652–661, https://doi.org/10.2320/matertrans.MB201805.
[43] O. Yamashita, S. Tomiyoshi, N. Sadatomi, J. Mater. Sci. 38 (2003) 1623–1629, https://doi.org/10.1023/A:1023251004461.
[44] M. Ohtaki, D. Ogura, K. Eguchi, H. Arai, Chem. Lett. 22 (1993) 1067–1070, https://doi.org/10.1246/cl.1993.1067.
[45] G. Li, W. Bai, N. Shi, Q. Fang, M. Xiong, J. Yang, Z. Ma, H. Rong, Eur. J. Mineral. 24 (2012) 1047–1052, https://doi.org/10.1127/0935-1221/2012/0024-2237.
[46] B.C. Sales, E.C. Jones, B.C. Chakoumakos, J.A. Fernandez-Baca, H.E. Harmon, J. W. Sharp, E.H. Volckmann, Phys. Rev. B 50 (1994) 8207–8213, https://doi.org/10.1103/PhysRevB.50.8207.
[47] Y. Dusausoy, J. Protas, R. Wandji, B. Roques, Acta Crystallogr. Sect. B Struct. Crystallogr. Cryst. Chem. 27 (1971) 1209–1218, https://doi.org/10.1107/S0567740871003765.
[48] X. Qu, S. Lü, J. Hu, Q. Meng, J. Alloy. Compd. 509 (2011) 10217–10221, https://doi.org/10.1016/j.jallcom.2011.08.070.
[49] K. Nogi, T. Kita, J. Mater. Sci. 35 (2000) 5845–5849, https://doi.org/10.1023/A:1026752206864.
[50] S.W. Kim, M.K. Cho, Y. Mishima, D.C. Choi, Intermetallics 11 (2003) 399–405, https://doi.org/10.1016/S0966-9795(03)00020-7.
[51] T. Kojima, K. Masumoto, M. Okamoto, I. Nishida, J. Less Common Met. 159 (1990) 299–305, https://doi.org/10.1016/0022-5088(90)90157-F.
[52] J. Hesse, R. Bucksch, J. Mater. Sci. 5 (1970) 272–273, https://doi.org/10.1007/BF00551006.
[53] M. Ito, H. Nagai, S. Katsuyama, K. Majima, J. Alloy. Compd. 315 (2001) 251–258, https://doi.org/10.1016/S0925-8388(00)01285-8.
[54] R.M. Ware, D.J. McNeill, Proc. Inst. Electr. Eng. 111 (1964) 178, https://doi.org/10.1049/piee.1964.0029.
[55] T. Takeuchi, New Thermoelectric Materials with Precisely Determined Electronic Structure and Phonon Dispersion, in: D.M. Rowe (Ed.), Thermoelectr. Its Energy Harvest, 1st ed., Taylor & Francis Group, Abingdon, UK, 2017, pp. 7–1-7–27, https://doi.org/10.1201/b11891.
[56] U. Birkholz, J. Schelm, Phys. Status Solidi 27 (1968) 413–425, https://doi.org/10.1002/pssb.19680270141.
[57] N.F. Mott, J. Non Cryst. Solids 1 (1968) 1–17, https://doi.org/10.1016/0022-3093(68)90002-1.
[58] M. Komabayashi, K.H. Ido, Jpn. J. Appl. Phys. 30 (1991) 331, https://doi.org/10.1143/JJAP.30.331.
[59] L.-D. Zhao, S.-H. Lo, J. He, H. Li, K. Biswas, J. Androulakis, C.-I. Wu, T.P. Hogan, D.-Y. Chung, V.P. Dravid, M.G. Kanatzidis, J. Am. Chem. Soc. 133 (2011) 20476–20487, https://doi.org/10.1021/ja208658w.
[60] X. Ai, B. Lei, M.O. Cichocka, L. Giebeler, R.B. Villoro, S. Zhang, C. Scheu, N. Pérez, Q. Zhang, A. Sotnikov, D.J. Singh, K. Nielsch, R. He, Adv. Funct. Mater. 33 (2023), https://doi.org/10.1002/adfm.202305582.
[61] R. Hanus, M.T. Agne, A.J.E. Rettie, Z. Chen, G. Tan, D.Y. Chung, M.G. Kanatzidis, Y. Pei, P.W. Voorhees, G.J. Snyder, Adv. Mater. 31 (2019) 1–10, https://doi.org/10.1002/adma.201900108.
[62] J.-H. Bahk, A. Shakouri, Appl. Phys. Lett. 105 (2014) 052106, https://doi.org/10.1063/1.4892653.
[63] J.J. Gong, A.J. Hong, J. Shuai, L. Li, Z.B. Yan, Z.F. Ren, J.-M. Liu, Phys. Chem. Chem. Phys. 18 (2016) 16566–16574, https://doi.org/10.1039/C6CP02057G.